Modeling Control and Simulation of a Power-Split Hybrid Wheel Loader

Davide Tebaldi[1] and Roberto Zanasi[2]

***Abstract*— This paper addresses the modeling control and simulation of a power-split hybrid propulsion system for driving a Wheel Loader. The modeling is performed exploiting the Power-Oriented Graphs (POG) graphical modeling technique. The main elements involved in the system are: an ICE (Internal Combustion Engine), two PMSMs (Permanent Magnet Synchronous Motors) controlled using a vectorial control and powered by a DC bus, a planetary gear set, a DC/DC converter, a supercapacitor acting as energy storage device and the transmission system of the vehicle, including all the physical elements from the gearbox to the vehicle wheels. A control strategy aiming at reducing the ICE operating point fluctuations caused by the transmission load and minimizing the ICE specific fuel consumption is proposed. Simulation results with reference to a typical driving cycle for this type of vehicle are finally presented and commented in detail.**

I. Introduction

The development of Hybrid Electric Vehicles (HEVs) represents an important area of research in the continuous effort to reduce the emissions of ICEs. This goal can be achieved thanks to the joint contribution of new HEV topologies and of suitable energy management strategies, which allow to maximize the benefits that the different HEV topologies can provide. From this consideration, it follows that the first necessary step to test a new HEV topology and the proposed energy management strategy is the effective modeling of the considered HEV topology. The modeling of HEVs, and of any physical element in general, can be made using many different approaches. When focusing on graphical modeling techniques, the three main categories available in the literature are Bond Graphs (BG) [1]-[2], Energetic Macroscopic Representation (EMR) [3]-[4] and Power-Oriented Graphs (POG) [5]-[6]. In [7], the vehicle modeling is performed using BG, while in [8] the modeling of different types of vehicles is performed using EMR. In [9]-[10], the modeling of HEVs is addressed using POG. The three techniques BG, EMR and POG offer different compromises between advantages and disadvantages [11].

In this paper, the modeling, control and simulation of a heavy-duty power-split HEV, that is a Hybrid Electric Wheel Loader (HEWL), are addressed by relying upon the POG technique. The latter is preferred thanks to some important characteristics, including the generation of block diagrams that are easily and directly implementable in the Simulink environment and the control on the power flows within the system.

Davide Tebaldi and Roberto Zanasi are with the Department of Engineering "Enzo Ferrari", University of Modena and Reggio Emilia, Modena, Italy, e-mail: davide.tebaldi@unimore.it, roberto.zanasi@unimore.it

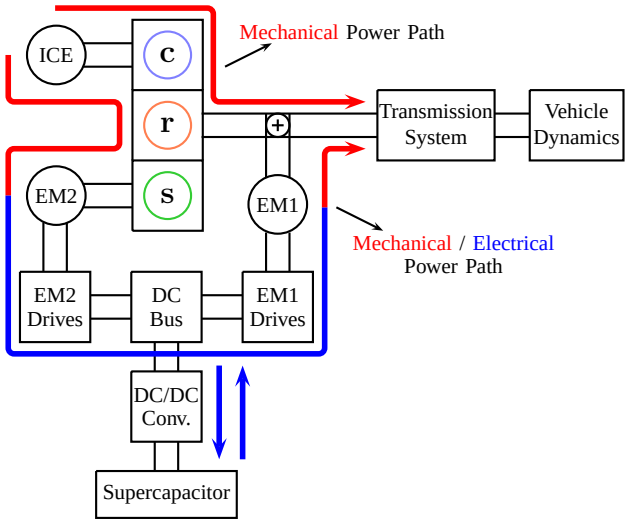

Fig. 1. Architecture of the considered power-split HEWL.

A schematic representation of the considered HEWL architecture is given in Fig. 1. From the figure, it is possible to notice the presence of three power sources: an ICE and two electric machines EM2 and EM1, connected to the carrier (C), sun (S) and ring (r) planetary gear set energetic ports, respectively. The transmission system of the vehicle is connected to the ring energetic port of the planetary gear set as well. The ICE is the main power source present on board the vehicle. The ICE generated power is going to be split into two power flows reaching the transmission system through two different power paths [12]. The first is highlighted in red in Fig. 1 and is a fully mechanical path, where a fraction of the ICE power is directly delivered to the transmission system through the planetary gear set. The second is highlighted in red / blue in Fig. 1 and is a hybrid mechanical / electrical path. In this case, a fraction of the ICE power gets absorbed by EM2 and stored in a supercapacitor through a DC/DC converter. The supercapacitor is ultimately used to power EM1 through the DC/DC converter and help drive the transmission system.

Once the modeling part has been addressed, a proper solution to the energy management problem must be found, that is how to properly control the three power sources to achieve the desired goals [13]-[18]. The main advantages of power-split HEVs are the decoupling of the ICE velocity and torque from the transmission velocity and load torque, which can be achieved thanks to the planetary gear set and the electric machines. The proposed solution for the energy management problem is based on the ICE *minimum specific consumption path* concept. This tool is introduced

in [9]-[10] for a power-split HEV and for a series HEV, and is extended in this paper to the power-split HEWL in Fig. 1. The objectives are to reduce the ICE operating point fluctuations caused by the transmission load in a traditional non-hybrid Wheel Loader architecture and the minimization of the ICE specific fuel consumption.

The remainder of the paper is structured as follows: Sec. II and the following subsections address the modeling of all the physical elements within the HEWL architecture in Fig. 1. Sec. III and the following subsections deal with the control of the three power sources to solve the energy management problem. Sec. IV presents the results of a simulation performed using a typical driving cycle for the considered type of vehicle. Finally, the conclusions of the paper are given in Sec. V.

II. Modeling of the Hybrid Topology

The Simulink implementation of the power-split HEWL architecture shown in Fig. 1 is reported in Fig. 2.

Moving from left to right, the physical elements present within the subsystems of Fig. 2 are: the electric machine EM2, the drives of EM2, the supercapacitor acting as energy storage device, the DC/DC converter, the DC bus, the drives of EM1, the electric machine EM1, the ICE, the planetary gear set, the transmission system and the vehicle dynamics. The magenta dashed lines in Fig. 2 highlight the *power sections* of the system. The product of the two power variables characterizing a power section has the physical meaning of the power flowing through the considered power section [6]. The system configuration shown in Fig. 2 directly points out the system power sections and is therefore said to be "power-oriented", which is why the POG technique allows a good control on the power flows within the system.

The considered electric machines EM1 and EM2 are PMSMs, and their modeling is addressed in Sec. II-A. The drives of EM1 and EM2 have been implemented using a vectorial control [19]. The vectorial control aims at minimizing the power dissipated because of the direct current component [20]. The supercapacitor and the DC bus have been modeled as two capacitors C_s and C_{dc}, characterized by the following first-order differential equations:

$$C_s\,\dot{V}_s = \hat{I}_L, \qquad C_{dc}\,\dot{V}_{dc} = I_{EM2} - I_{EM1} + (-I_L), \tag{1}$$

where V_s and V_{dc} are the voltages across C_s and C_{dc}, $\hat{I}_L$ is the load current I_{EM2}–I_{EM1} up-converted, I_{EM2} and I_{EM1} are the EM2 and EM1 currents after AC/DC conversion and $-I_L = -(I_{EM2} - I_{EM1})$. The DC/DC converter is supposed to be lossless and is modeled as a logical Matlab function that down-converts voltage V_{dc} to voltage $V_s < V_{dc}$ and up-converts the load current $I_{EM2} - I_{EM1}$ to the load current $\hat{I}_L > I_{EM2} - I_{EM1}$. The modeling of the power-split device, namely the considered planetary gear set, is performed in Sec. II-B. The modeling of the transmission system and of the vehicle dynamics is addressed in Sec. II-C. The ICE is modeled within the "ICE" subsystem in Fig. 2 as a lookup table saturating the output torque to the maximum ICE torque versus speed, whereas the ICE control is discussed in Sec. III-A.

A. PMSM Modeling

Under the hypothesis of sinusoidal rotor flux and star-connected stator phases, the dynamic equations [6], [20] describing the PMSM in a rotating d-q frame, namely a reference frame rotating together with the rotor rotation, are:

$$\begin{bmatrix} p\,L_{se} & 0 & 0 \\ 0 & p\,L_{se} & 0 \\ 0 & 0 & J_M \end{bmatrix} \begin{bmatrix} \dot{I}_d \\ \dot{I}_q \\ \dot{w}_m \end{bmatrix} = \begin{bmatrix} -p\,R_s & p^2 w_m L_{se} & 0 \\ -p^2 w_m L_{se} & -p\,R_s & -K_q \\ 0 & K_q & -b_M \end{bmatrix} \begin{bmatrix} I_d \\ I_q \\ w_m \end{bmatrix} + \begin{bmatrix} V_d \\ \bar{V}_q \\ -\bar{\mathrm{T}}_e \end{bmatrix},$$

$$\text{where:} \quad \begin{cases} \bar{V}_q = V_q \;-\; R_{sq}\,\mathrm{sgn}\,({}^{\omega}I_q)\;{}^{\omega}I_q^2, \\ \bar{\mathrm{T}}_e = \mathrm{T}_e \;+\; b_c\,\mathrm{sgn}(\omega_m) + b_{Mq}\,\mathrm{sgn}(\omega_m)\,{\omega_m}^2. \end{cases}$$

The parameter p is the number of polar pairs, $L_{se} = L_s + (1/2)M_{s0}$, being L_s and M_{s0} the stator phase self-inductance coefficient and the maximum value of mutual inductance between stator phases, whereas J_M is the motor inertia. The parameter R_s is the stator phase resistance, K_q is the in-quadrature component of the torque vector (also known as the torque constant) and b_M is the rotor friction coefficient. The variable w_m is the motor velocity, whereas I_d, I_q, V_d, V_q are the direct and in-quadrature components of the current and voltage vectors, and T_e the motor load torque. The parameters R_{sq}, b_c and b_{Mq} are the Joule losses term, the Coulomb friction coefficient and the parameter accounting for the impact of the air friction losses. Thanks to the vectorial control [19], the tracking errors between the actual values of two current components I_d and I_q and the values demanded by the control tend to zero as first order systems with settling time τ_s. The actual system parameters values for the two industrial PMSMs employed in this project to play the roles of EM1 and EM2 have been estimated from the machines datasheet using the estimation approach based on the analysis of the system power efficiency, see [21]-Sec. IV-D.

B. Planetary Gear Set Modeling

A schematic representation of the considered planetary gear set is shown in the upper part of Fig. 3. The modeling has been addressed exploiting the systematic methodology proposed in [22]-[24]. The system state-space model [6] is:

$$\begin{cases} \mathbf{L}\,\dot{\mathbf{x}} = \mathbf{A}\,\mathbf{x} + \mathbf{B}\,\mathbf{u}, \\ \mathbf{y} = \mathbf{B}^{\mathrm{T}}\,\mathbf{x}, \end{cases} \quad \mathbf{A} = \begin{bmatrix} -\mathbf{B}_J - \mathbf{R}^{\mathrm{T}}\mathbf{B}_K\mathbf{R} & -\mathbf{R}^{\mathrm{T}} \\ \mathbf{R} & \mathbf{0} \end{bmatrix},$$
$$\mathbf{L} = \begin{bmatrix} \mathbf{J} & \mathbf{0} \\ \mathbf{0} & \mathbf{K}^{-1} \end{bmatrix}, \quad \mathbf{B} = \begin{bmatrix} \mathbf{I} \\ \mathbf{0} \end{bmatrix}, \quad \mathbf{x} = \begin{bmatrix} \mathbf{w} \\ \mathbf{F} \end{bmatrix}, \quad \begin{matrix} \mathbf{y} = \mathbf{w}, \\ \mathbf{u} = \mathbf{T}. \end{matrix} \tag{2}$$

where $\mathbf{A}$ is the power matrix, $\mathbf{L}$ is the energy matrix, $\mathbf{B}$ is the input matrix, $\mathbf{x}$ is the state vector, $\mathbf{F}$ is the force vector, $\mathbf{y} = \mathbf{w}$ is the output velocity vector and $\mathbf{u} = \mathbf{T}$ is the input torque vector. This model can be graphically described and directly implemented in Simulink using the general POG model valid for any planetary gear set [22]-[24] reported in the lower

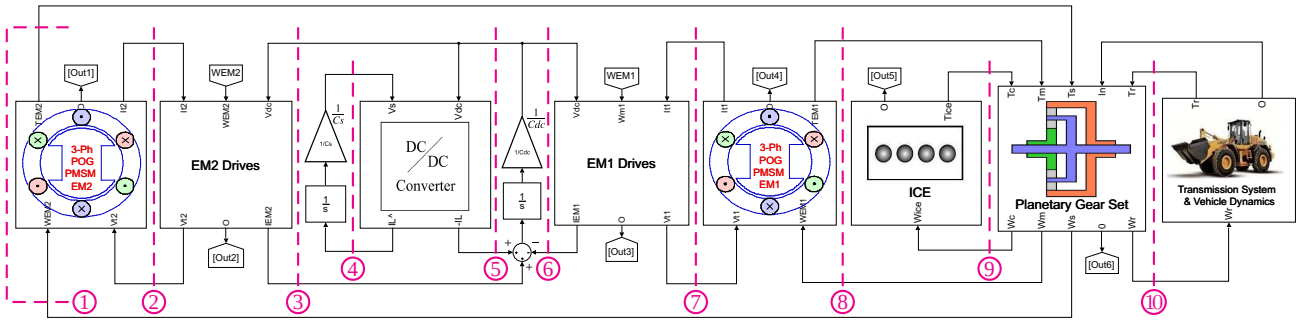

Fig. 2. Simulink implementation of the considered power-split HEWL.

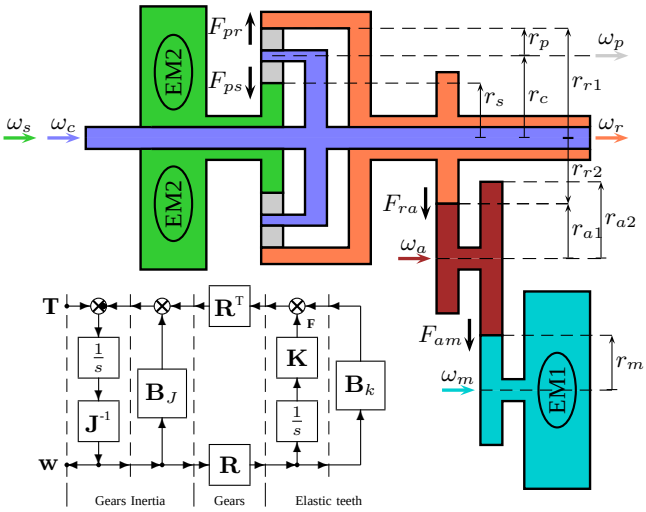

Fig. 3. Structure and POG model of the considered planetary gear set.

part of Fig. 3. The velocity vector $\mathbf{w}$, the torque vector $\mathbf{T}$, the inertia matrix $\mathbf{J}$ and the inertia friction matrix $\mathbf{B}_J$ are:

$$\mathbf{w}=\begin{bmatrix} w_c \\ w_p \\ w_s \\ w_r \\ w_a \\ w_m \end{bmatrix} \mathbf{T}=\begin{bmatrix} \mathrm{T}_c \\ \mathrm{T}_p \\ \mathrm{T}_s \\ \mathrm{T}_r \\ \mathrm{T}_a \\ \mathrm{T}_m \end{bmatrix} \mathbf{J}=\begin{bmatrix} J_c & 0 & 0 & 0 & 0 & 0 \\ 0 & J_p & 0 & 0 & 0 & 0 \\ 0 & 0 & J_s & 0 & 0 & 0 \\ 0 & 0 & 0 & J_r & 0 & 0 \\ 0 & 0 & 0 & 0 & J_a & 0 \\ 0 & 0 & 0 & 0 & 0 & J_m \end{bmatrix} \mathbf{B}_J=\begin{bmatrix} b_c & 0 & 0 & 0 & 0 & 0 \\ 0 & b_p & 0 & 0 & 0 & 0 \\ 0 & 0 & b_s & 0 & 0 & 0 \\ 0 & 0 & 0 & b_r & 0 & 0 \\ 0 & 0 & 0 & 0 & b_a & 0 \\ 0 & 0 & 0 & 0 & 0 & b_m \end{bmatrix}.$$

The force vector $\mathbf{F}$, the stiffness matrix $\mathbf{K}$ and the stiffness friction matrix $\mathbf{B}_K$ are:

$$\mathbf{F}=\begin{bmatrix} \mathrm{F}_{ps} \\ \mathrm{F}_{pr} \\ \mathrm{F}_{ra} \\ \mathrm{F}_{am} \end{bmatrix} \mathbf{K}=\begin{bmatrix} K_{ps} & 0 & 0 & 0 \\ 0 & K_{pr} & 0 & 0 \\ 0 & 0 & K_{ra} & 0 \\ 0 & 0 & 0 & K_{am} \end{bmatrix} \mathbf{B}_K=\begin{bmatrix} b_{ps} & 0 & 0 & 0 \\ 0 & b_{pr} & 0 & 0 \\ 0 & 0 & b_{ra} & 0 \\ 0 & 0 & 0 & b_{am} \end{bmatrix}.$$

The radius matrix $\mathbf{R}$ uniquely defining the system, see [22]-Sec.III-A, is:

$$\mathbf{R}=\begin{bmatrix} r_c & -r_p & -r_s & 0 & 0 & 0 \\ r_c & r_p & 0 & -r_{r1} & 0 & 0 \\ 0 & 0 & 0 & -r_{r2} & -r_{a1} & 0 \\ 0 & 0 & 0 & 0 & -r_{a2} & -r_m \end{bmatrix}.$$

The following constraints among the radii within matrix $\mathbf{R}$ and Fig. 3 hold: $r_c = r_p + r_s$ and $r_{r1} = 2\,r_p + r_s$. When $\mathbf{K} \to \infty$ in system (2), one obtains four constraints relating the six angular velocities in vector $\mathbf{w}$. Keeping ω_c and ω_r as independent state variables, the following state-space transformation can be used on system (2):

$$\underbrace{\begin{bmatrix} \mathbf{w} \\ \mathbf{F} \end{bmatrix}}_{\mathbf{x}} = \underbrace{\begin{bmatrix} \mathbf{Q}_1 \\ \mathbf{0} \end{bmatrix}}_{\mathbf{T}_1} \underbrace{\begin{bmatrix} w_c \\ w_r \end{bmatrix}}_{\mathbf{x}_1}, \; \mathbf{Q}_1=\begin{bmatrix} 1 & -\dfrac{r_c}{r_p} & \dfrac{2\,r_c}{r_s} & 0 & 0 & 0 \\ 0 & \dfrac{r_{r1}}{r_p} & -\dfrac{r_{r1}}{r_s} & 1 & -\dfrac{r_{r2}}{r_{a1}} & \dfrac{r_{a2}\,r_{r2}}{r_{a1}\,r_m} \end{bmatrix}^{\mathrm{T}}, \quad (3)$$

in order to obtain the following reduced model:

$$\underbrace{\begin{bmatrix} J_1 & J_3 \\ J_3 & J_2 \end{bmatrix}}_{\mathbf{L}_1} \underbrace{\begin{bmatrix} \dot{\omega}_c \\ \dot{\omega}_r \end{bmatrix}}_{\dot{\mathbf{x}}_1} = \underbrace{\begin{bmatrix} b_1 & b_3 \\ b_3 & b_2 \end{bmatrix}}_{\mathbf{A}_1} \underbrace{\begin{bmatrix} \omega_c \\ \omega_r \end{bmatrix}}_{\mathbf{x}_1} + \underbrace{\mathbf{Q}_1^{\mathrm{T}}}_{\mathbf{B}_1} \underbrace{\mathbf{T}}_{\mathbf{u}}, \quad (4)$$

where $\mathbf{L}_1 = \mathbf{T}_1^{\mathrm{T}}\mathbf{L}\mathbf{T}_1$, $\mathbf{A}_1 = \mathbf{T}_1^{\mathrm{T}}\mathbf{A}\mathbf{T}_1$ and $\mathbf{B}_1 = \mathbf{T}_1^{\mathrm{T}}\mathbf{B}$. The reduced order model (4) allows for effective simulations with no loss of information [23]-[24] and is the one employed in this paper to simulate the considered planetary gear set. Note that, by neglecting the dissipative terms within matrix $\mathbf{A}_1$ in (4) and assuming the system at steady-state, one obtains $\mathbf{Q}_1^{\mathrm{T}}\mathbf{T} = 0 \leftrightarrow \mathbf{T} \in \ker(\mathbf{Q}_1^{\mathrm{T}})$. Since no input torque is applied to the planet gear and to gear a, see Fig. 3, it follows that $\mathrm{T}_p = \mathrm{T}_a = 0$, which means that $\mathbf{Q}_1^{\mathrm{T}}\mathbf{T} = 0$ leads to the following steady-state torque constraints:

$$\mathrm{T}_c + \frac{2\,r_c}{r_s}\mathrm{T}_s = 0, \quad -\frac{r_{r1}}{r_s}\mathrm{T}_s + \mathrm{T}_r + \frac{r_{a2}\,r_{r2}}{r_{a1}\,r_m}\mathrm{T}_m = 0. \quad (5)$$

C. Transmission System and Vehicle Modeling

The Simulink implementation of the vehicle transmission system is reported inside the subsystem called "Transmission System & Vehicle Dynamics" in Fig. 2. The structure of the considered transmission system is schematized in Fig. 4, whereas the corresponding POG model [10] is reported in Fig. 5. Indeed, the input section in the POG

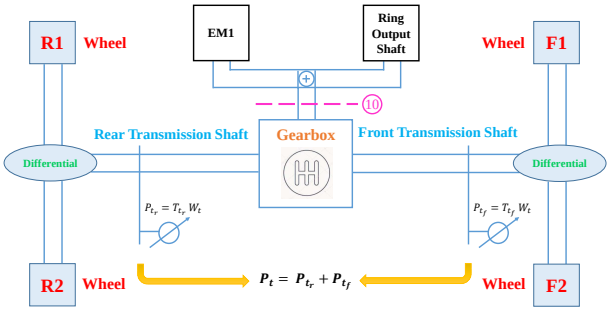

Fig. 4. Structure of the considered vehicle transmission system.

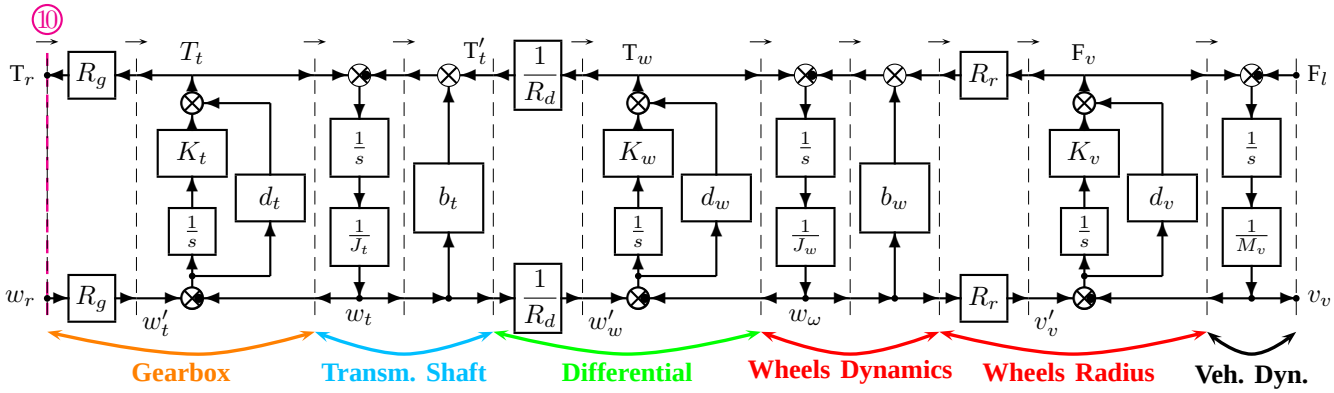

Fig. 5. POG block scheme of the considered vehicle transmission system.

model of Fig. 5, denoted as section ⑩, coincides with the corresponding sections in Fig. 2 and Fig. 4. The two power variables characterizing section ⑩ are the ring load torque T_r and the ring speed w_r. The part highlighted in orange in Fig. 4 and Fig. 5 is the Gearbox, where the time-variant connection block characterized by parameters $R_g \in \{1/r_{1b}; 1/r_{2b}; 1/r_{3b}; 1/r_{1f}; 1/r_{2f}; 1/r_{3f}; 1/r_{4f}\}$ models the gearshifting mechanism, being r_{1b}, r_{2b}, r_{3b} the first, second and third backward gear ratios and r_{1f}, r_{2f}, r_{3f}, r_{4f} the first, second, third and fourth forward gear ratios. The torsional spring characterized by stiffness coefficient K_t accounts for the gearbox elasticity, whereas the dissipative element d_t accounts for the energy loss occurring during the transient. The Transmission Shaft part highlighted in lightblue accounts for the rear and front transmission shafts: J_t is the moment of inertia and b_t is a linear friction coefficient. The part highlighted in green is the Differential; its contribution is accounted for by parameter R_d, together with a rotational spring K_w accounting for the intrinsic elasticity and its friction coefficient d_w. The two parts highlighted in red account for the Wheels Dynamics, where J_w is the equivalent moment of inertia of the four wheels and b_w is a linear friction coefficient, and for the Wheels Radius R_r, with the rotational spring K_v and the friction coefficient d_v accounting for the intrinsic wheels elasticity and for the transient losses. The final part describes the Vehicle Dynamics, where parameter M_v is the vehicle mass. The external force F_l accounts for the load force that the vehicle is subject to during its operation.

III. Energy Management Problem

This section focuses on the description of the adopted solution for the energy management problem, by describing the control applied to the three power sources: the ICE in Sec. III-A, EM2 in Sec. III-B and EM1 in Sec. III-C.

A. ICE Control

Thanks to the planetary gear set, the ICE velocity is decoupled from the transmission velocity. This makes it possible to apply a speed control to the ICE. The goal is to make the ICE work in the least consumption regions of the specific fuel consumption map. A useful tool that can be used for this purpose is the *ICE minimum specific consumption path*, giving the ICE operating point $(w_{ice}, \mathrm{T}_{ice} = \mathrm{T}_c)$ ensuring the least consumption for the considered ICE desired power. Once the *ICE minimum specific consumption path* is computed, see [9]-Sec. III-A, one obtains the magenta path on the ICE specific fuel consumption map shown in Fig. 6:

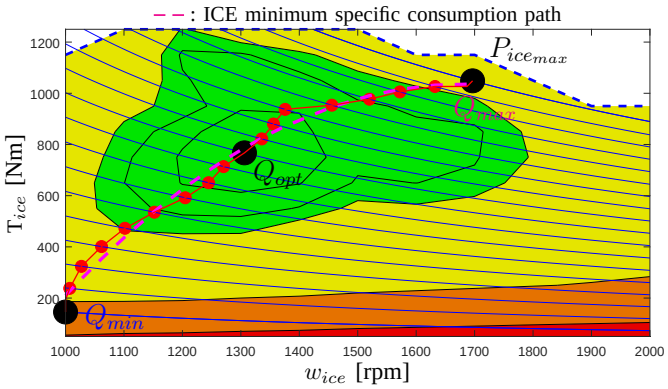

Fig. 6. ICE specific consumption map on the operating plane $(w_{ice}, \mathrm{T}_{ice})$.

$$\mathrm{T}_{ice} = a_0 + w_{ice} a_1 + w_{ice}^2 a_2, \text{ where } \begin{cases} a_0 = -4.01 \cdot 10^3 \\ a_1 = 57.41 \\ a_2 = -0.16 \end{cases}, \quad (6)$$

The desired ICE operating point is chosen on the *minimum specific consumption path*, see [9]-(5), as follows:

$$(w_{ice_{des}}, \mathrm{T}_{ice_{des}}) = \begin{cases} Q_{opt} & \text{if } V_{s_{low}} < V_s < V_{s_{up}} \\ Q_{req} & \text{if } V_s \le V_{s_{low}} \text{ until } V_s = V_{s_{ref}} \\ Q_{max} & \text{if } V_s \le V_{s_{min}} \text{ until } V_s = V_{s_{ref}} \\ Q_{min} & \text{if } V_s \ge V_{s_{up}} \text{ until } V_s = V_{s_{ref}} \end{cases}, \quad (7)$$

where $V_{s_{min}}$, $V_{s_{low}}$, $V_{s_{ref}}$ and $V_{s_{up}}$ are the minimum, lower, reference and upper thresholds of supercapacitor voltage V_s:

$$V_{s_{min}} < V_{s_{low}} < V_{s_{ref}} < V_{s_{up}}, \qquad V_{s_{ref}} = \frac{V_{s_{low}} + V_{s_{up}}}{2}.$$

The operating points Q_{opt}, Q_{req}, Q_{max} and Q_{min}, see [9]-Sec. III-A, correspond to the following power variables:

$$Q_{opt} = \left(w_{ice_{opt}}, \mathrm{T}_{ice_{opt}}\right), \quad Q_{req} = \left(w_{ice_{req}}, \mathrm{T}_{ice_{req}}\right),$$
$$Q_{max} = \left(w_{ice_{max}}, \mathrm{T}_{ice_{max}}\right), \quad Q_{min} = \left(w_{ice_{min}}, \mathrm{T}_{ice_{min}}\right).$$

Fig. 6 shows that the operating points Q_{opt}, Q_{max} and Q_{min} belong to the *minimum specific consumption path* of the ICE. The *required operating point* $Q_{req} = \left(w_{ice_{req}}, \mathrm{T}_{ice_{req}}\right)$,

when $V_s \leq V_{s_{low}}$, is computed as follows:

1) $\Delta_P = \dfrac{\Delta_E}{\Delta_T} = \dfrac{\frac{1}{2} C_s V_{s_{ref}}^2 - \frac{1}{2} C_s V_{s_{low}}^2}{\Delta_T}$,
2) $P_{ice_{req}} = P_{ice_{opt}} + \Delta_P = w_{ice_{opt}} \mathrm{T}_{ice_{opt}} + \Delta_P$,
3) $w_{ice_{req}} = k_1 P_{ice_{req}} + k_2 = 0.43 \cdot 10^{-3} P_{ice_{req}} + 93.16$,
4) $\mathrm{T}_{ice_{req}} = a_0 + w_{ice_{req}} a_1 + w_{ice_{req}}^2 a_2$,

where Δ_P is the ICE required extra power, t_{low} is the time instant when $V_s = V_{s_{low}}$, t_{ref} is the time instant when $V_s = V_{s_{ref}}$, k_1 and k_2 describe a linear dependence between $w_{ice_{req}}$ and $P_{ice_{req}}$, and the function in step 4) is the one in (6). Once the desired ICE speed $w_{ice_{des}} \in \{w_{ice_{min}}, w_{ice_{opt}}, w_{ice_{req}}, w_{ice_{max}}\}$ is computed using (7), the ICE speed control is applied employing the following regulator:

$$\mathrm{T}_{ice} = \left(\frac{K_{P_{ice}} + K_{P_{ice}} K_{I_{ice}} s}{K_{I_{ice}} s} \right) (w_{ice_{des}} - w_{ice}), \quad (8)$$

where $K_{P_{ice}}$ and $K_{I_{ice}}$ are two design parameters. The torque $\mathrm{T}_{ice} = \mathrm{T}_c$ is then applied to the carrier energetic port of the planetary gear set in Fig. 3.

B. EM2 Control

A torque control is applied to EM2. The desired EM2 torque $\mathrm{T}_{EM2_{des}}$ is therefore given by:

$$\mathrm{T}_{EM2_{des}} = \left(\frac{K_{P_2} + K_{P_2} K_{I_2} s}{K_{I_2} s} \right) (\mathrm{T}_{ice} - \mathrm{T}_{ice_{des}}), \quad (9)$$

where K_{P_2} and K_{I_2} are two design parameters. The desired EM2 torque $\mathrm{T}_{EM2_{des}}$ is then used as a control signal for the vectorial control [19] implemented within the subsystem "EM2 Drives" in Fig. 2. The resulting EM2 output torque $\mathrm{T}_{EM2} = \mathrm{T}_s$ is applied to the sun energetic port of the planetary gear set in Fig. 3. Note that the purpose of the EM2 control is to ensure that the ICE torque $\mathrm{T}_{ice} = \mathrm{T}_c$ coincides with the desired one $\mathrm{T}_{ice_{des}}$, which is chosen as the currently optimal one according to rule (7) on the *minimum specific consumption path*.

C. EM1 Control

The EM2 torque control determines the EM2 torque $\mathrm{T}_{EM2} = \mathrm{T}_s$ to guarantee $\mathrm{T}_{ice} = \mathrm{T}_c = T_{ice_{des}}$ through (9), where $T_{ice_{des}}$ is given by (7). Given that the EM2 torque $\mathrm{T}_{EM2} = \mathrm{T}_s$ is determined, according to the second equation in (5), the EM1 torque $\mathrm{T}_{EM1} = \mathrm{T}_m$ is the only one left to compensate for the remaining fraction of the transmission load torque T_r, which is given by the external load force F_l and by the friction coefficients in the transmission POG model in Fig. 5. From (3), it results that any two out of the six planetary gear angular velocities uniquely determine the remaining ones. The ICE speed control described in Sec. III-A determines the ICE speed $w_{ice} = w_c$. A speed control is then applied to EM1 in order to determine the desired EM1 speed $w_{EM1_{des}} = w_{m_{des}}$ that makes the transmission follow the desired transmission speed $w_{r_{des}}$:

$$w_{EM1_{des}} = w_{r_{des}} \left(\frac{r_{a2}\, r_{r2}}{r_{a1}\, r_m} \right). \quad (10)$$

The desired EM1 torque $\mathrm{T}_{EM1_{des}}$ is determined using the following regulator:

$$\mathrm{T}_{EM1_{des}} = \left(\frac{K_{P_1} + K_{P_1} K_{I_1} s}{K_{I_1} s} \right) (w_{EM1_{des}} - w_{EM1}), \quad (11)$$

where K_{P_1} and K_{I_1} are two design parameters. The desired EM1 torque $\mathrm{T}_{EM1_{des}}$ is then used as a control signal for the vectorial control [19] implemented within the subsystem "EM1 Drives" in Fig. 2. The resulting EM1 output torque $\mathrm{T}_{EM1} = \mathrm{T}_m$ is applied to the gear m energetic port of the planetary gear set in Fig. 3, and is going to compensate for the remaining fraction of the transmission load torque T_r which is not compensated by the ICE torque $\mathrm{T}_{ice} = \mathrm{T}_c$.

PMSMs	
p	4
L_{se}	32.68 [μH]
J_M	0.22 [kg m^2]
R_s	0.95 [m Ω]
K_q	0.65 [Nm/A]
b_M	$1 \cdot 10^{-3}$ [(Nm s)/rad]
R_{sq}	2.64 [nV/A^2]
b_c	0.83 [μNm]
b_{Mq}	$3.4 \cdot 10^{-9}$ [Nm s^2/rad^2]
Planetary Gear Set	
J_c	0.047 [kg m^2]
J_p	$0.63 \cdot 10^{-3}$ [kg m^2]
J_s	$0.67 \cdot 10^{-3}$ [kg m^2]+J_M
J_r	0.06 [kg m^2]
J_a	$8.6 \cdot 10^{-3}$ [kg m^2]
J_m	$0.45 \cdot 10^{-3}$ [kg m^2]+J_M
$b_c \ldots b_m$	$1.4 \cdot 10^{-3}$ [(Nm s)/rad]
r_c	7.5 [cm]
r_p	3.4 [cm]
r_s	4.2 [cm]
r_{r1}	11 [cm]
r_{r2}	4.6 [cm]
r_{a1}	2.64 [cm]
r_{a2}	4.6 [cm]
r_m	2.4 [cm]
ICE Control	
$K_{P_{ice}}$	220
$K_{I_{ice}}$	1.87
PMSM: Vectorial Control	
τ_s	3 [ms]

Transmission and Vehicle	
r_{1b}	3.251
r_{2b}	1.822
r_{3b}	0.945
r_{1f}	3.145
r_{2f}	1.984
r_{3f}	1.272
r_{4f}	0.936
K_t	$4.01 \cdot 10^7$ [Nm/rad]
d_t	305.6 [Nm s/rad]
J_t	$1.5 \cdot 10^{-3}$ [kg m^2]
b_t	2.4 [(Nm s)/rad]
R_d	21.22
K_w	$= K_t$
d_w	$= d_t$
J_w	$4.25 \cdot 10^3$ [kg m^2]
b_w	24 [(Nm s)/rad]
R_r	0.58 [m]
K_v	$6.2 \cdot 10^6$ [N/m]
d_v	$284.5 \cdot 10^3$ [N s/m]
M_v	$14.4 \cdot 10^3 \rightarrow 18.4 \cdot 10^3$ [kg]
EM2 Control	
K_{P_2}	35
K_{I_2}	0.17
EM1 Control	
K_{P_1}	80.75
K_{I_1}	0.49
Supercapacitor	
C_s	50 [F]
DC Link	
C_{dc}	10 [mF]

TABLE I

PARAMETERS OF THE CONSIDERED ARCHITECTURE.

IV. Simulation Case Study

The architecture of the HEWL reported in Fig. 2 has been simulated in Matlab/Simulink with reference to a typical driving cycle for this type of vehicle. The simulation has been performed using the architecture parameters shown in Tab. I and starting from zero initial conditions, expect for the initial carrier and ICE speed $w_{ice_0} = w_{ice_{opt}} = 1306$ [rpm] and the initial supercapacitor and DC bus voltages $V_{s_0} = 700$ [V] and $V_{dc_0} = 750$ [V]. The desired vehicle speed profile is shown in blue dashed line in the first subplot of Fig. 8. The load force profile that the vehicle experiences during its operation, applied as a signal F_l in the transmission system POG block scheme in Fig. 5, is shown in black dashed line in the third subplot of Fig. 8. During the considered driving cycle, the Wheel Loader starts digging to load the

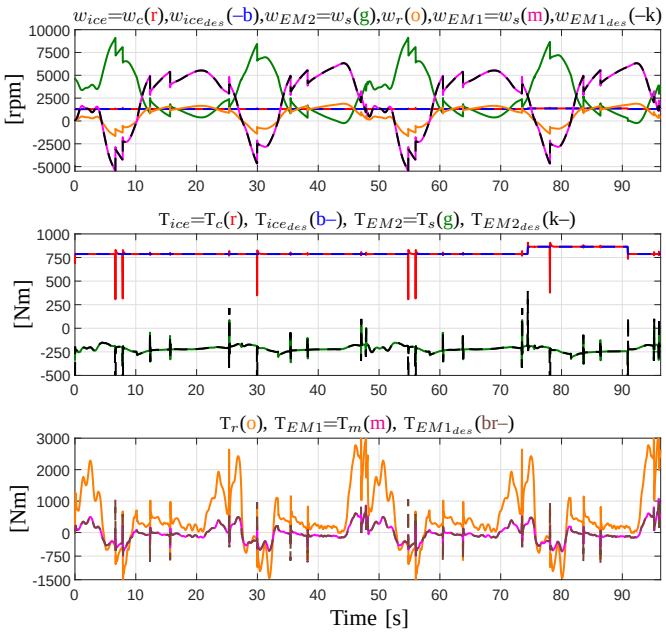

Fig. 7. Planetary gear set angular velocities and torques.

bucket before time instant t_1 and starts unloading the bucket at time instant t_2. The same operation is repeated at time instants t'_1 and t'_2. The time instants t_1, t_2, t'_1 and t'_2 are highlighted in the first subplot of Fig. 8 by four red spots. The change of mass following the Wheel Loader loading and unloading the bucket at the considered time instants is accounted for by making the vehicle mass M_v change from $14.4 \cdot 10^3$ [kg] (empty bucked) to $18.4 \cdot 10^3$ [kg] (full bucked) when $t \in (t_1, t_2) \bigvee t \in (t'_1, t'_2)$ and viceversa, as reported in Tab. I. The hydraulic load that the Wheel Loader is subject to during the considered driving cycle, which includes the power needed to power the mechanical arm loading the bucket, is given by the power profile P_{pp} shown in violet in the third subplot of Fig. 8. The power profile P_{pp} is divided by the DC bus voltage V_{dc} in order to originate an "equivalent load current" to be added to I_{EM1} in (1), thus accounting for the additional power from the supercapacitor requested by the hydraulic load. Note that all the main load contributions that one might encounter on the field have been accounted for in the simulation: the external load force profile F_l experienced by the vehicle, the vehicle mass change caused by the Wheel Loader loading and unloading the bucket, and the "equivalent load current" accounting for the additional power required to power the mechanical arm moving the bucket. The simulation results are shown in Fig. 7, Fig. 8 and Fig. 9. The first subplot of Fig. 7 shows the angular velocities of the planetary gear set inertial elements. From the good matching between the desired and actual ICE and EM1 speeds $w_{ice_{des}}$, $w_{ice} = w_c$, $w_{EM1_{des}}$, $w_{EM1} = w_m$, it is possible to notice the effectiveness of the speed control applied to the two elements ICE and EM1. The second and third subplots of Fig. 7 show the input torques of the planetary gear set inertial elements. The good matching between the desired and actual EM1 torques $\mathrm{T}_{EM1_{des}}$, $\mathrm{T}_{EM1} = \mathrm{T}_m$ highlights the effectiveness of the speed and vectorial control applied to EM1, whereas the good matching between the desired and

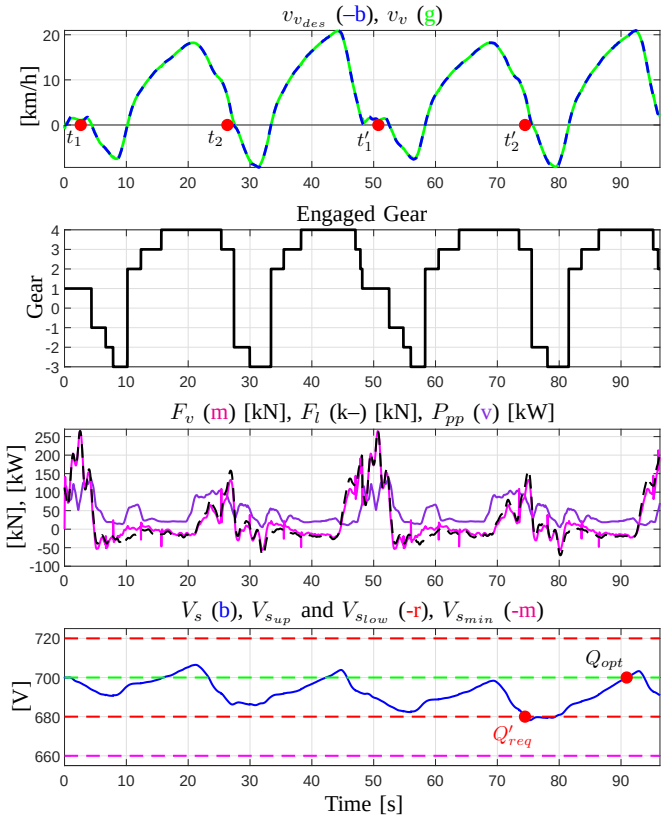

Fig. 8. Vehicle Speed; Engaged Gear; Wheels Force and Pumps Power; Supercapacitor Voltage.

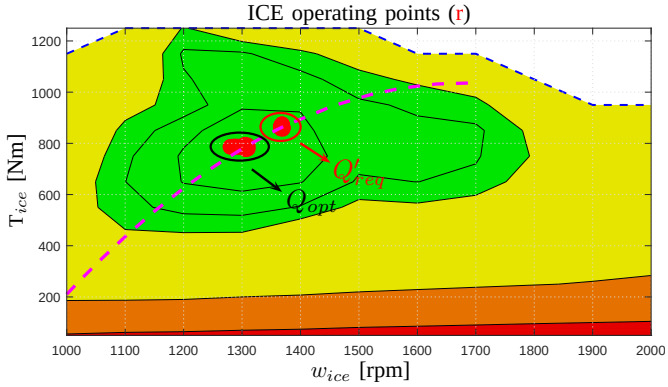

Fig. 9. ICE operating points on ICE specific consumption map.

actual ICE and EM2 torques $\mathrm{T}_{ice_{des}}$, $\mathrm{T}_{ice} = \mathrm{T}_c$, $\mathrm{T}_{EM2_{des}}$, $\mathrm{T}_{EM2} = \mathrm{T}_s$ highlights the effectiveness of the torque and vectorial control applied to EM2. The subplots of Fig. 8 show, from top to bottom, the desired and actual vehicle speeds, the engaged gear, the vehicle motive and load forces, the pumps power profile and the supercapacitor voltage. The DC bus voltage V_{dc} is not shown since it remains constant as required, whereas the pumps load current and the EM1 and EM2 load/generated currents are eventually absorbed from the supercapacitor. From the first subplot, it is indeed possible to see that the Wheel Loader follows the desired speed profile. From the third subplot, one can notice a peak in the load force F_l before time instants t_1 and t'_1, which are due to the Wheel Loader digging to load the bucket. Fig. 9 shows the ICE operating points at steady-state on the 2D operating plane $(w_{ice}, \mathrm{T}_{ice})$ showing the ICE specific

fuel consumption map. The fourth subplot of Fig. 8 shows that the behavior of the supercapacitor voltage V_s during the simulation causes two changes of the ICE operating point according to (7): Q'_{req} is a required operating points on the ICE *minimum specific consumption path* called by the condition $V_s < V_{s_{low}}$ when occurring, whereas Q_{opt} is indeed the optimal operating point in the middle of the least consumption area in Fig. 9. The ICE operating point is equal to Q_{opt} at the beginning of the simulation as initial condition and at steady state when condition $V_s = V_{s_{ref}}$ is verified once again after the operating point Q'_{req} was called. From Fig. 7 and Fig. 9, it is possible to see that the ring load torque T_r fluctuations due to the operation of the considered heavy-duty vehicle, such as the peaks of load torque when digging for example, are now compensated by the joint contribution of the EM1 torque $\mathrm{T}_{EM1} = \mathrm{T}_m$ and of the ICE torque $\mathrm{T}_{ice} = \mathrm{T}_c$, the latter always confined on the ICE *minimum specific consumption path* thanks to the action of EM2. This allows to reduce the fluctuations of the ICE operating point during the considered driving cycle, leading to a more comfortable driving experience. Metrics providing the comparison of the ICE specific fuel consumption with respect to the one given by the traditional non-hybrid Wheel Loader could not be reported in this paper because of industrial secret reasons. Nevertheless, Fig. 9 shows that the ICE operating point coincides with the optimal one Q_{opt} for as long as possible and, in any case, it never leaves the ICE *minimum specific consumption path* at steady state. Furthermore, note that the calculations required by the presented control strategy are contained, which makes it interesting for real-time implementation.

V. Conclusions

In this paper, the modeling, control and simulation of a power-split hybrid electric Wheel Loader have been studied. The modeling of all the physical elements involved in the considered hybrid architecture has been performed using the Power-Oriented Graphs modeling technique, which allows to build block schemes that are easily and directly implementable in the Simulink environment. A solution for the energy management problem has been proposed, allowing to reduce the ICE operating point fluctuations associated with the vehicle operation and to minimize the ICE specific fuel consumption. The control of the three power sources in the considered architecture has then been described, and the effectiveness of the proposed solution has been tested with the aid of some simulation results with reference to a typical driving cycle for the considered heavy-duty vehicle.

References

[1] H. M. Paynter, “Analysis and design of engineering systems”, MIT-press, Camb., MA, 1961.

[2] D. C. Karnopp, D. L. Margolis and R. C. Rosenberg “System dynamics - modeling and simulation of mechatronic systems”, Wiley Interscience, ISBN 0-471-33301-8, 3rd ed. 2000.

[3] A. Bouscayrol, B. Davat, B. de Fornel, B. Francois, J. P. Hautier, F. Meibody-Tabar and M. Pietrzak-David, “Multimachine multiconverter system: application for electromechanical drives”, Eur. Physics Journal - Appl. Physics, vol. 10, no. 2, pp. 131-147, May 2000.

[4] J. C. Mercieca, J. N. Verhille and A. Bouscayrol, “Energetic macroscopic representation of a subway traction system for a simulation model”, IEEE-ISIE’04, Ajaccio, May 2004, pp. 1519-1524.

[5] R. Zanasi, “Power oriented modelling of dynamical system for simulation”, IMACS Symp. on Modelling and Control of Technological System, Lille, France, May 1991.

[6] R. Zanasi, “The power-oriented graphs technique: system modeling and basic properties”, IEEE Vehicle Power and Propulsion Conference, Lille, France, September 1-3, 2010.

[7] M. Cipek, J. Deur and J. Petrić, “Bond graph analysis of power flow in series-parallel hybrid electric vehicle transmissions”, UKACC International Conference on Control, Coventry, UK, September 7-10, 2010.

[8] K. Chen, A. Bouscayrol, A. Berthon, P. Delarue, D. Hissel and R. Trigui, “Global modeling of different vehicles using energetic macroscopic representation”, IEEE Vehicle Power and Propulsion Conference (VPPC), Harbin, China, September 3-5, 2008.

[9] D. Tebaldi and R. Zanasi, “Modeling and control of a power-split hybrid propulsion system”, IEEE 45th Annual Conference of the Industrial Electronics Society, Lisbon, Portugal, October 14-17, 2019.

[10] D. Tebaldi and R. Zanasi, “Modeling control and simulation of a series hybrid propulsion system”, Vehicular Power and Propulsion Conference (VPPC), Gijón, Spain, Oct. 26-29, 2020.

[11] R. Zanasi, G. H. Geitner, A. Bouscayrol and W. Lhomme, “Different energetic techniques for modelling traction drives”, 9th International Conference on Modeling and Simulation of Electric Machines, Converters and Systems (ELECTRIMACS), Québec, Canada, June 8-11, 2008.

[12] J. M. Miller, “Hybrid electric vehicle propulsion system architectures of the e-CVT type”, IEEE Trans. on Power Electronics, May. 2006.

[13] R. E. Bellman, Dynamic Programming. Princeton, NJ, USA: Princeton Univ. Press, 1957.

[14] G. Paganelli, G. Ercole, A. Brahma, Y. Guezennec and G. Rizzoni, “General supervisory control policy for the energy optimization of charge-sustaining hybrid electric vehicles”, JSAE Rev., vol. 22, no. 4, pp. 511-518, 2001.

[15] J. Liu and H. Peng, “Control optimization for a power-split hybrid vehicle”, American Control Conference (ACC), Minneapolis, Minnesota, USA, June 14-16, 2006.

[16] N. Kim, S. Cha and H. Peng, “Optimal control of hybrid electric vehicles based on pontryagin’s minimum principle”, IEEE Trans. Control Syst. Technol., vol. 19, no. 5, pp. 1279-1287, Sep. 2011.

[17] J. Wu, J. Ruan, N. Zhang and P. D. Walker, “An optimized real-time energy management strategy for the power-split hybrid electric vehicles”, IEEE Trans. Veh. Technol., vol. 27, no. 3, pp. 1194-1202, May 2019.

[18] G. Buccoliero, P. G. Anselma, S. A. Bonab, G. Belingardi and A. Emadi, “A new energy management strategy for multimode power-split hybrid electric vehicles”, IEEE Trans. Veh. Technol., vol. 69, no. 1, pp. 172-181.

[19] R. Zanasi and F. Grossi, “Vectorial control of multi-phase synchronous motors using POG approach”, 35th Annual Conference of IEEE Industrial Electronics, Porto, Portugal, November 3-5, 2009.

[20] M. Fei, R. Zanasi and F. Grossi, “Modeling of multi-phase permanent magnet synchronous motors under open-phase fault condition”, IEEE International Conference on Control and Automation (ICCA), Santiago, Chile, December 19-21, 2011.

[21] R. Zanasi and D. Tebaldi, “Power flow efficiency of linear and non-linear physical systems”, IEEE European Control Conference (ECC), Naples, Italy, June 25-28, 2019.

[22] R. Zanasi and D. Tebaldi, “Planetary gear modeling using the power-oriented graphs technique”, IEEE European Control Conference (ECC), Naples, Italy, Jun. 25-28, 2019.

[23] R. Zanasi and D. Tebaldi, “Power-oriented modeling of epicyclic gear trains”, Vehicular Power and Propulsion Conference (VPPC), Gijón, Spain, Oct. 26-29, 2020.

[24] R. Zanasi and D. Tebaldi, “Modeling of complex planetary gear sets using power-oriented graphs”, IEEE Trans. Veh. Technol., vol. 69, no. 12, pp. 14470-14483, Dec. 2020.